C. R. Mecanique 346 (2018) 1055–1071

Contents lists available at ScienceDirect

Comptes Rendus Mecanique

www.sciencedirect.com

Computational methods in welding and additive manufacturing/Simulation numérique des procédés de soudage et de fabrication additive

Numerical modelling of fluid and solid thermomechanics in additive manufacturing by powder-bed fusion: Continuum and level set formulation applied to track- and part-scale simulations

Yancheng Zhang, Qiang Chen, Gildas Guillemot, Charles-André Gandin, Michel Bellet *

MINES ParisTech, PSL Research University, Centre de mise en forme des matériaux (CEMEF), CNRS UMR 7635, CS 10207, 06904 Sophia Antipolis cedex, France

ARTICLE INFO

Article history:
Received 21 March 2018
Accepted 18 April 2018
Available online 3 September 2018

Keywords:
Additive manufacturing
Powder-bed fusion
Finite element modelling
Level set formulation
Continuum assumption
Thermomechanics
Track and part scales

ABSTRACT

The thermomechanical analysis of powder-bed fusion using a laser beam is simulated in both meso- and macroscales within a framework combining continuum assumption and level-set formulation. The mesoscale simulation focuses on laser interaction with the powder bed, and on subsequent melting and solidification. Modelling is conducted at the scale of material deposition, in which powder-bed fusion, hydrodynamics in the melt pool, and thermal stress are simulated. The macroscale model focuses on part construction and post-deposition. During construction, by contrast with the mesoscale approach, the fluid flow in the fusion zone is ignored and material addition is simplified by modelling it at the scale of entire layers, or fractions of layers. The modelling of the energy input is adapted accordingly. This thermomechanical model addresses heat exchange, residual stress, and distortion at the part's scale. In both approaches, adaptive remeshing is applied, providing a good compromise between the needs to provide accurate prediction and maintaining sustainable computation times.

0. Introduction

Additive manufacturing (AM) consists in building a part layer by layer directly from the data of a 3D computer-aided design (CAD) model. As such, and contrary to traditional manufacturing approaches, it may offer a customized design for complex geometries in a rapid design-to-manufacture cycle [1]. Selective laser melting (SLM, also called laser beam melting, LBM) and electron beam melting (EBM) are two powder-bed AM techniques. As both processes can fabricate quasi-fully dense near-net-shape components and are suitable for various metallic powders, great interests are received from both industrial and academic fields [2]. The present paper deals with SLM, but most of the modelling concepts presented here could be adapted to EBM.

* Corresponding author.
E-mail address: michel.bellet@mines-paristech.fr (M. Bellet).

https://doi.org/10.1016/j.crme.2018.08.008

Powder-bed fusion AM still suffers from defects having a thermomechanical origin, such as porosities and cracking. Cracks may consist of solidification cracks that form at the rear of the fusion zone, which undergoes tensile stress during cooling. Cracks may also form in the solid state, at lower temperature, as a result of the stress build-up in the part under construction. An additional effect of such build-up of thermal stresses is the distortion of the part, which is of course an issue as it affects the capacity of obtaining a good geometrical accuracy on the final product. In total, process control is difficult to optimize in order to manufacture sound and high-precision near-net-shape parts. To minimize costly trial-and-error approach of AM processes by repeated experiments, numerical simulation has been introduced and continuously developed to model the thermal and mechanical responses during and after processing. Up to now, this has been done at different scales, as detailed hereunder.

A first class of numerical models directly addresses the particles' scale. Studies focus on laser/matter interaction, melting of particles, formation of the fusion zone, and thermohydraulics. Körner and co-workers have developed a particle scale numerical model based on the Lattice–Boltzmann method with a volume of fluid approach for free surfaces [3]. Recently, they applied their model to the study of the influence of the stochastic powder bed on the EBM process window for dense parts [4]. By use of an adequate method to model the formation of 100 layers with their 2D approach, simulations show a good agreement with the experimental statistical occurrence of porosities, and with the surface roughness for the samples produced. Still by particle-scale modelling, King et al. [5] simulated track formation in LBM at the particle scale with and without surface tension by coupling thermal diffusion with hydrodynamics using finite-volume/finite-element implementation. They found that considering surface tension tends to provide smoother melt pools and improved heat transfer with the substrate. Qiu et al. [6] developed a hydrodynamic numerical simulation based on the finite volume method, including surface tension, Marangoni force, and recoil pressure associated with vaporization. They applied their model to a powder bed of very small dimensions consisting of 50 to 60 regularly packed Ti-6Al-4V powder particles. They found that the driving forces are responsible for melt pool instability leading to melt splashing, which could explain the occurrence of porosities. A similar method is adopted by Megahed et al. [7] and Mindt et al. [8] in particle scale, different samples of powder beds being considered to investigate the influence of the powder bed structure on the processed surface. Ly et al. [9] used and developed a finite element (FE) model, but in an Arbitrary Lagrangian–Eulerian (ALE) formulation. They carried out particle-scale simulations of LBM, on a slightly more extended powder bed (about two hundred particles). The model is capable of simulating the ejection of molten droplets from the melt pool, as a result of the intense liquid flow prevailing there. Besides, the authors explain the denudation process by metal-vapour-driven particle entrainment. As it can be seen from the previous references, particle-scale models are well suited to model particle motion, fluid flow in the melt pool, and phenomena like liquid spattering and porosity formation. However, they have not been applied yet to the modelling of thermomechanics-driven defects such as distortions, and different types of cracking.

A second class of numerical models addresses the part scale. These macroscale approaches are more specifically dedicated to part distortions and stress build-up. In the macro scale, the details of the local laser/matter interaction, and of the local fluid flow in the fusion zone are ignored. Efforts are focused on modelling heat transfer and mechanical response at the scale of the part. Modelling techniques are generally based on the FE method in a Lagrangian framework, and matter deposition is simulated by element activation or element birth techniques. Many FE thermomechanical models have been developed using this approach, and only a few contributors will be mentioned here. Among them, Gu and He [10] used a commercial three-dimensional transient FE software, with the element activation technique. They simulated the formation of three parallel tracks scanned back and forth. The calculated stress distribution was in agreement with the location of the cracks in experiments. With a similar numerical method, Hodge et al. [11] studied the issue of the change in thermal distribution and melt pool extension during the addition of overhang regions, which are regions non-supported by pre-deposited tracks, but supported by non-consolidated powder. They showed that the method could be applied to the scale of a small part of the order of 1 mm^3 consisting of a dozen of layers, for the prediction of residual stress and distortion. However, when element activation is applied to simulate the exact laser scan path like in the two latter studies, modelling LBM processing of real components is out of reach due to prohibitive computational times. In order to keep calculation times sustainable, the build-up of parts is often simulated by adding all the powder elements in one layer simultaneously – or even in groups of several layers [12] – at the top of the construction. In the recent period, significant efforts have been done to reduce computational times. The inherent strain method has been developed by Alvarez et al. [13]. They demonstrated that the proposed model is possible to accurately predict the distortion induced by different scanning strategy in short times. In addition, Li et al. [14] have developed a practical multi-scale modelling methodology for fast prediction of part distortion by integrating a microscale laser scan model, a mesoscale layer hatch model, and a macroscale part model. A concept of equivalent heat source has been developed based on the microscale laser scan model. By using the equivalent heat source, local residual stress field was predicted in the mesoscale layer hatch model. The residual stress field was then imported to the macroscale model to predict part distortion and residual stress.

In this paper, an original method is presented, which is based on finite elements in a level-set formulation and can be applied to both track and part scale. The method has been first developed by Chen et al. [15] at the track scale. Contrary to particle-scale methods, the powder bed is considered as a continuum enduring continuous evolution when being transformed in a dense melt, and further solidified. The formation of the melt pool, the hydrodynamics and the resulting shapes of the deposited tracks can be simulated. In the present paper, the extension of the method to solid thermomechanics will be presented. The same FE–level-set method was adapted to macroscale simulations, first to model heat transfer [16], and more recently to model thermomechanics. The paper aims at giving a unified presentation of this method. It is organized

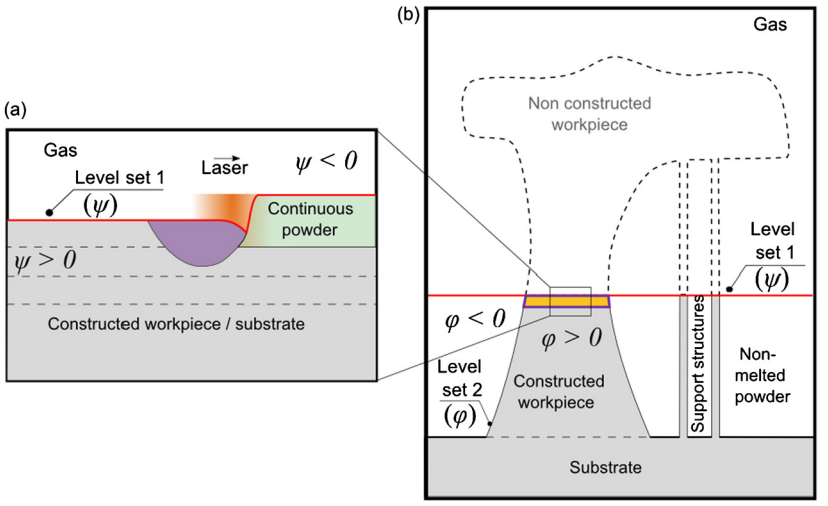

Fig. 1. Interfaces tracked by the level-set method in the context of the LBM process. : a) and b) (red color lines) the gas/material interface (ψ), and b) the non-melted powder/constructed part interface (φ).

as follows. Firstly, the level-set framework used to track interfaces is introduced. Secondly, the governing equations for both thermal and mechanical analysis are given. Finally, numerical simulations dedicated to the prediction of thermo-mechanical fields in both track and part scales are presented, illustrating the capacity and the potential of the method. A final section consists in a discussion of the main common and differentiated features of track-scale and part-scale applications of the method.

1. Level-set formulation in the context of powder-bed fusion

1.1. Level-set description of interfaces

The level-set (LS) method [17] is commonly used to identify and track an interface inside a continuum Ω, the latter being spatially discretized using the FE method. The interface is defined by the isovalue $\psi = 0$, where $\psi = \psi(\boldsymbol{x}, t)$ is the signed distance function to the interface at any location $\boldsymbol{x}$ in the continuum, and at any instant t. Hence, on both sides of the interface, a region Ω_1 is such that $\psi < 0$ while the complementary part Ω_2 checks $\psi > 0$. Along this interface, a transition zone with half-thickness ϵ can be defined, ϵ being a small positive value. A Heaviside function, $\mathcal{H}$, is then defined, which varies continuously within this transition zone, from 0 in Ω_1 to 1 in Ω_2:

$$\mathcal{H}(\psi) = \begin{cases} 0 & \psi < -\epsilon \\ \frac{1}{2}\left[1 + \frac{\psi}{\epsilon} + \frac{1}{\pi}\sin\left(\frac{\pi\psi}{\epsilon}\right)\right] & |\psi| \leq \epsilon \\ 1 & \psi > \epsilon \end{cases} \tag{1}$$

In the transition zone, any physical property χ is averaged according to the following expression, providing a continuous variation between its value in Ω_1 and Ω_2 regions:

$$\{\chi\} = \mathcal{H}\chi^{D_2} + (1 - \mathcal{H})\chi^{D_1} \tag{2}$$

1.2. Interface tracking in LBM numerical simulation

In LBM numerical simulation, interest is to track two kinds of interfaces, as illustrated in Fig. 1: on one hand, the gas/material interface, and on the other hand the interface separating the dense consolidated material from the non-consolidated powder material.

1.2.1. Gas/material interface

The identification and tracking of this interface is essential in both the meso- and the macroscale analyses. This interface is designed in red colour in Fig. 1 and separates domains having large differences in intrinsic properties: the metallic material on one side, and the gas domain on the other side.

In the mesoscale analysis (Fig. 1a) the material is shown in three different states: powder, liquid, and dense solid states. Note that those three states do not require additional level-set systems to separate and differentiate them. Indeed, the transition from the powder state to the liquid state is triggered above a certain fusion temperature, and is not revertible.

In addition, the transition from the liquid state to the solid state is supposed to occur in a certain temperature interval, in which the liquid fraction changes according to solidification equations. In such state transitions, the physical properties of the material are homogenized according to averaging laws considering the local volume fraction of each state: powder state, liquid state, and dense solid state. Details are provided in Chen et al. [15]. In the mesoscale analysis, the time evolution of this interface is essential as it determines the final shape of the track, which results from the hydrodynamic flow taking place in the fusion zone, and from subsequent solidification. Having solved for the velocity field $\boldsymbol{v}$ in the whole domain Ω, the signed distance function ψ has to be computed at each time step, providing an updating of the interface for $\psi = 0$. Different techniques can be used to proceed with the updating of the whole field ψ. The method used by Chen et al. [15] consists in solving first the following transport equation,

$$\frac{\partial \psi}{\partial t} + \boldsymbol{v} \cdot \nabla \psi = 0 \tag{3}$$

Then a full reconstruction of the field ψ is made by a simple geometrical method, which is initiated from the new position of the interface resulting from Eq. (3).

In the macroscale analysis (Fig. 1b), the interest is not focused on a precise description of the shape of the elementary tracks. Therefore, material addition is considered at the scale of an entire layer, or a fraction of a layer. In this case, the level set associated with the material/gas interface only serves for the expression of the continuous variation of the physical properties in the transition zone close to the interface. The updating of the level-set function ψ depends only on the construction speed and the CAD geometry previously defined before computation. In such conditions, the update of its position does not result from a transport equation such as Eq. (3).

1.2.2. Interface between part and powder

Another interface to be considered in the macroscale analysis is the one defined between the part under construction, made of dense solid material (in grey colour, bottom of Fig. 1), and the material remaining in the powder state because it has not been irradiated by the laser. This requires an additional level-set function, which is denoted as φ. Based on this second level-set function φ, conformed meshes can be obtained from the meshing/remeshing procedure named FITZ, not presented in the present paper. Details on this remeshing strategy are provided in references [16,18].

2. Governing equations

The main equations governing thermomechanics in powder-bed fusion are introduced hereafter. It should be underlined that the equations are presented in their generic form, which is used either in the meso- or the macroscopic approach. Specific points regarding each of them when used in each of the two approaches will be presented further, in Sections 3 and 4.

2.1. Heat transfer

In the framework of the level-set formulation, the non-steady energy conservation equation is the following:

$$\frac{\partial \{\rho h\}}{\partial t} + \nabla \cdot \left(\{\rho h\}\boldsymbol{v}\right) - \nabla \cdot \left(\{\lambda\}\nabla T\right) = \dot{Q} \tag{4}$$

where $\{\rho h\}$ and $\{\lambda\}$ stand for the interface mixed values (Eq. (2)) of the volumetric enthalpy and of the thermal conductivity, respectively. T denotes the temperature field and $\dot{Q}$ is a right-hand-side source or sink term that will be further presented and discussed in the meso- and macroscopic contexts.

2.2. Mass conservation

The mass conservation equation is considered in order to ensure material continuity:

$$\frac{\partial \{\rho\}}{\partial t} + \nabla \cdot \left(\{\rho\}\boldsymbol{v}\right) = 0 \tag{5}$$

2.3. Fluid flow

Actually, the dynamics of the molten zone is ignored when proceeding to the macroscale analysis of the process. Consequently, fluid flow modelling is restricted to the sole mesoscopic approach. The momentum equation for fluid flow is the following:

$$\{\rho\}\left[\frac{\partial \boldsymbol{v}}{\partial t} + (\nabla \boldsymbol{v})\boldsymbol{v}\right] = \nabla \cdot [-p\mathbf{I} + \mathbf{s}] + \{\rho\}\boldsymbol{g} + \boldsymbol{f}_v \tag{6}$$

where p denotes the pressure, $\mathbf{I}$ is the identity tensor, $\boldsymbol{g}$, the gravity vector and $\boldsymbol{f}_v$ is a body force that will be detailed hereafter. The tensor $\mathbf{s}$ is the deviatoric part of the Cauchy stress tensor, and is related to the velocity field $\boldsymbol{v}$ by a compressible Newtonian behaviour that is expressed by:

$$\mathbf{s} = 2\{\mu\}\left(\dot{\boldsymbol{\epsilon}} - \frac{1}{3}\operatorname{tr}(\dot{\boldsymbol{\epsilon}})\mathbf{I}\right) \tag{7}$$

where $\{\mu\}$ is the averaged dynamic viscosity of the fluid, and $\dot{\boldsymbol{\epsilon}}$ is the strain-rate tensor:

$$\dot{\boldsymbol{\epsilon}} = \frac{1}{2}\left(\nabla\boldsymbol{v} + (\nabla\boldsymbol{v})^{\mathsf{T}}\right) \tag{8}$$

The use of a compressible behaviour model will be further commented in more details.

2.4. Solid mechanics

In the context of additive manufacturing, inertia effects can be neglected, and the momentum equation governing the material in the solid state can be written as:

$$\nabla\cdot\boldsymbol{\sigma} + \rho\boldsymbol{g} = 0 \tag{9}$$

where $\boldsymbol{\sigma}$ denotes the Cauchy stress tensor. Because the solid-state material must be considered on the very large temperature range – from room to fusion temperature – its behaviour is modelled using an elastic–viscoplastic constitutive model. The constitutive equations are the following ones:

$$\dot{\boldsymbol{\epsilon}} = \dot{\boldsymbol{\epsilon}}^{\mathrm{el}} + \dot{\boldsymbol{\epsilon}}^{\mathrm{vp}} + \dot{\boldsymbol{\epsilon}}^{\mathrm{th}} \tag{10}$$

$$\dot{\boldsymbol{\epsilon}}^{\mathrm{el}} = \frac{1+\nu}{E}\dot{\boldsymbol{\sigma}} - \frac{\nu}{E}\operatorname{tr}(\dot{\boldsymbol{\sigma}})\mathbf{I} \tag{11}$$

$$\dot{\boldsymbol{\epsilon}}^{\mathrm{vp}} = \frac{\sqrt{3}}{2\overline{\sigma}}\left[\frac{\overline{\sigma} - \sigma_{\mathrm{Y}}}{\sqrt{3}K_{\mathrm{vp}}\overline{\varepsilon}^{n}}\right]_{+}^{\frac{1}{m}}\mathbf{s} \tag{12}$$

$$\dot{\boldsymbol{\epsilon}}^{\mathrm{th}} = -\frac{1}{3\rho}\frac{\mathrm{d}\rho}{\mathrm{d}t}\mathbf{I} \tag{13}$$

In Eq. (10), the strain rate tensor $\dot{\boldsymbol{\epsilon}}$ is split into an elastic part $\dot{\boldsymbol{\epsilon}}^{\mathrm{el}}$, a viscoplastic part $\dot{\boldsymbol{\epsilon}}^{\mathrm{vp}}$, and a thermal part $\dot{\boldsymbol{\epsilon}}^{\mathrm{th}}$. The latter includes the thermal expansion as expressed in Eq. (13). Equation (11) expresses the hypoelastic Hooke's law where E denotes the Young's modulus and ν the Poisson's coefficient. Equation (12) expresses the viscoplastic flow rule: the viscoplastic strain rate derives from a potential (not expressed here, depending on the stress tensor) and is found proportional to the stress deviator $\mathbf{s}$ by the so-called normality rule. σ_{Y} denotes the static yield stress below which no viscoplastic deformation occurs (the expression between the square brackets reduces to zero when negative). As a consequence of the previous expressions, the relationship between the von Mises equivalent stress $\overline{\sigma}$ and the equivalent strain rate $\dot{\overline{\varepsilon}}$ is:

$$\overline{\sigma} = \sigma_{\mathrm{Y}} + K_{\mathrm{vp}}\left(\sqrt{3}\right)^{m+1}\overline{\varepsilon}^{n}\dot{\overline{\varepsilon}}^{m} \tag{14}$$

It can be noted that when writing equations from (10) to (13), level set averaging $\{\cdot\}$ has been forgotten. Indeed, when solving solid-state mechanics, each finite element (see next section) is considered as totally belonging either to the constructed part, or to the gas and powder domains. In the first case, the constitutive equations (10)–(13) apply, with material properties depending on temperature. In the second case (gas and powder domains), an incompressible Newtonian constitutive model applies, derived from Eq. (7). According to this strategy, and contrary to what is done when solving the fluid problem, nodal level-set averaging is not used.

2.5. Finite element discretization

For the sake of simplicity and conciseness, the weak form and the FE discretization of the above conservation equations are not detailed in the present paper. Regarding the heat transfer problem, the weak form at the mesoscale directly derives from the work of Saad et al. [19]. The details of the weak form for the macroscale resolution can be found in the work of Zhang et al. [20]. Regarding the fluid flow problem, the interested reader may refer to [15], in which the weak form is fully detailed, and to [21] for a presentation of the finite element discretization. As for the solid mechanics problem, equivalent information can be found in [22,23].

3. Meso-scale modelling at the scale of material deposition

The mesoscale modelling presented in this paper has been first developed and applied in the context of powder-bed fusion process applied to ceramic materials. This induces some specific features regarding the laser energy input that will be presented hereunder. Comments will also be provided regarding the melting stage of the powder bed and its modelling. Applications of the modelling will be then presented and discussed.

3.1. Model setting

3.1.1. Laser–matter interaction

When processing ceramic materials – alumina in the present case – with a near-infrared laser, like Yb:YAG with wavelength of 1070 nm, the interaction between laser and ceramic material is totally different to metals. Pure alumina is indeed almost "transparent" to this radiation, leading to a lower absorption and a larger penetration depth of radiations. The absorption efficiency can be improved by adding energy absorbers such as carbon and SiC, as proposed by Moniz et al. [24], but even in this case such a laser radiation propagates deeply in the ceramics. In order to include this effect in mesoscale simulations, a heat source model based on Beer–Lambert law is proposed, expressing a local contribution to the heat source term $\dot{Q}$ in Eq. (4) as [15]:

$$\dot{Q}_L(r,z) = (1-R)\phi_0(r)\alpha \exp\left(-\int_0^z \alpha \, \mathrm{d}l\right) \tag{15}$$

where R denotes the reflection coefficient, α the in-depth absorption coefficient of the material, r the distance to the laser beam axis, z the distance to the material surface exposed to the laser. It is assumed that the distribution of the surface power in the transverse section of the beam is of Gaussian type:

$$\phi_0(r) = \frac{2P_{\mathrm{L}}}{\pi r_{\mathrm{int}}^2} \exp\left(-\frac{2r^2}{r_{\mathrm{int}}^2}\right) \tag{16}$$

with P_{L} the laser power, and r_{int} the effective interaction radius. The integral term in Eq. (15) reflects the variation of the absorption coefficient α with the material state and temperature. In addition, no absorption is assumed in the gas domain. In order to consider the absorbing path, the integral along the vertical z direction is computed onto a regular grid covering the region impacted by the laser. Integral terms are consequently estimated at the nodes of this specific grid before reassignment onto the nodes of the FE mesh, where source terms (Eq. (15)) are then computed. Considering the optical specialty of alumina and the use of absorbents, the effective absorption coefficient, α, obviously plays a key role in laser–matter interaction and should be properly identified as possibly done by inverse approach [25].

3.1.2. Powder-bed melting

For fluid flow analysis in the mesoscopic modelling, the material obeys the Newtonian behaviour law expressed by Eq. (7) whatever its state: powder bed, liquid, or dense solid. The three states are characterized by viscosities having different orders of magnitude, and depending on temperature. This temperature dependence also allows treating the transition from a porous powder bed to the dense liquid state. In a certain temperature interval around the fusion temperature, the powder medium is supposed to condense and melt. As a consequence, the density is increased by a factor 2 as a porosity fraction of 50% is assumed in the present simulations, inducing a convergent velocity field due to mass conservation: Eq. (5).

3.1.3. Heat transfer and fluid flow

In such SLM processes, it is commonly considered that the main driving forces inducing fluid flow in the molten pool derive from surface tension as encountered in welding processes. Actually surface tension induces two driving forces. A first one is normal to the liquid surface and proportional to its total curvature. A second surface force acts in the tangential plane and consists of the tangential gradient of the first one. Significant values of these tangential forces, also named Marangoni forces, are expected owing to the temperature dependency of the surface tension and the tangential gradient of temperature. The surface tension ($\boldsymbol{T}_{\mathrm{s}}$) and Marangoni forces ($\boldsymbol{T}_{\mathrm{m}}$) should be distinguished in Eq. (17):

$$\boldsymbol{T}_{\mathrm{s}} = \gamma\kappa\boldsymbol{n} \qquad \boldsymbol{T}_{\mathrm{m}} = \frac{\partial\gamma}{\partial T}\nabla_s T \tag{17}$$

where γ denotes the surface tension, κ the total curvature, $\boldsymbol{n}$ the unit normal vector to the liquid surface, and ∇_s the tangential operator along this surface. In the context of a level-set formulation, these surface forces need to be converted into volume forces, by multiplying them by the Dirac function (defined as $\delta = \partial\mathcal{H}/\partial\psi$). As such, they are implemented, in the 2 ϵ-thick neighbourhood of the liquid/gas interface, as contributions of the right-hand side body forces $\boldsymbol{f}_v$ in Eq. (6) [15].

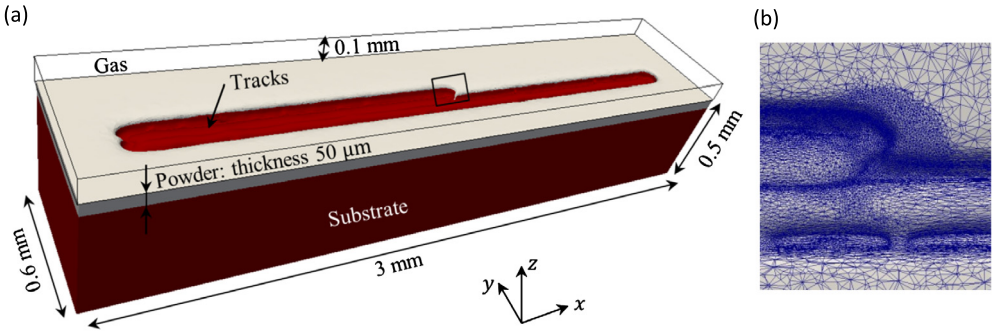

Fig. 2. a) Simulated system in the case of multitrack deposition. b) Zoom with top view showing the adapted mesh around the laser irradiated zone (black rectangle on the central region of a)).

Table 1
Parameters used in simulations developed to follow track evolution during SLM process [25,28].

	Section 3.2.1	Section 3.2.2	Section 3.3
	Fluid and heat transfer	Track and layer surface shape	Solid thermomechanics
v_L (mm s^{-1})	200	400 or 600	300
r_{int} (μm)	37.5	64.6	37.5
α_s (mm^{-1})	5	8.98	5
α_l (mm^{-1})	5	3.88	5
$\partial\gamma/\partial T$ ($\times 10^{-5}$ N m^{-1} K^{-1})	−48 or 48	8.2	8.2

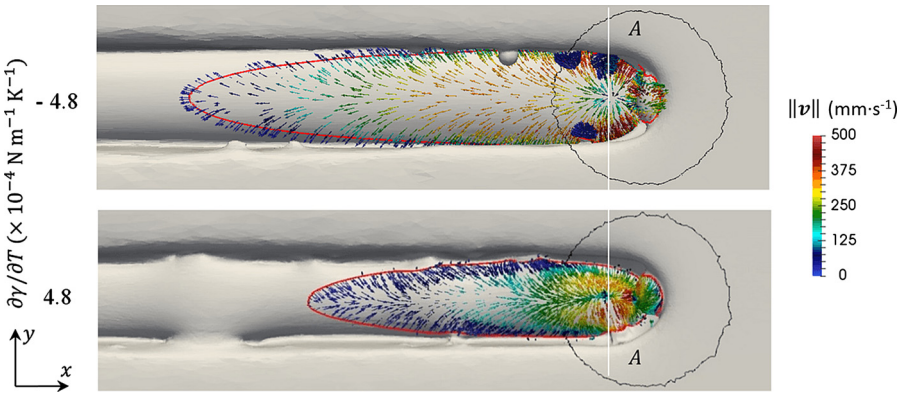

Fig. 3. Top view of melt pool (red contour) and liquid velocity field arrows when the laser (black contour) arrives to $x = 1.42$ mm for cases with different $\partial\gamma/\partial T$.

3.2. Application to powder-bed fusion of alumina

Simulations are carried out in a system illustrated in Fig. 2 for the case of multitrack deposition. The material domain is composed of a substrate and a layer of powder deposited on it, leading to a total height of 0.5 mm. A laser of power 84 W scans from $x = 0.2$ mm to $x = 2.8$ mm in each pass. The mesh is adapted in order to follow the evolving gas/material interface, principally based on the metric constructed by error estimation. The result is shown in the right part of the figure: good representation of track surface is achieved. For single track deposition, the width of the system is 0.5 mm and the height of the material domain is 1 mm.

Different parameters are used in the following simulations, as listed in Table 1. Note that the absorption coefficient used in the heat source model may be distinguished between powder, solid, and liquid states as demonstrated previously. In the present simulations, a unique value is used for powder and solid states. In addition, for cases in Sections 3.2.1 and 3.3, it is proposed to use also identical value for all three states in order to investigate the sensibility to material properties in fluid dynamics and heating mode in mechanical solution. For the solid thermomechanics, the driving force is the density variation during heating and cooling. A linear density evolution from 3970 to 3780 kg m^{-3} [26] is used from ambient temperature to liquidus. The constitutive law is taken from Sanchez-Gonzalez et al. [27] and is based on results of compression tests.

3.2.1. Fluid and heat transfer

Fig. 3 shows the influence of Marangoni effect by varying the temperature dependency of surface tension corresponding to the coefficient $\partial\gamma/\partial T$, from the extreme value of -4.8×10^{-4} N m^{-1} K^{-1} reported in the literature [28] to its opposite

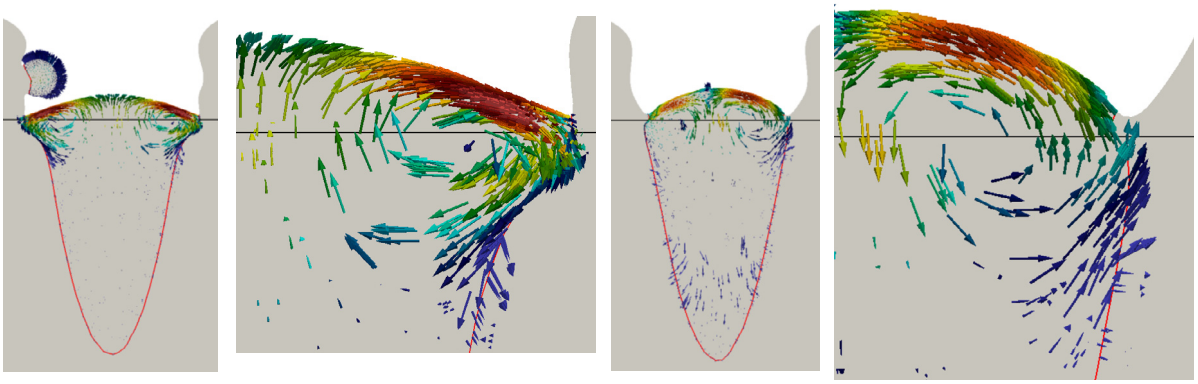

Fig. 4. Melt pool geometry (red contour) and liquid velocity field in transverse sections A–A (as defined in Fig. 3) for cases with different $\partial\gamma/\partial T$. The black line indicates the initial powder/substrate interface. For each case, a zoom is given showing the liquid flow in the top-right region of the melt pool.

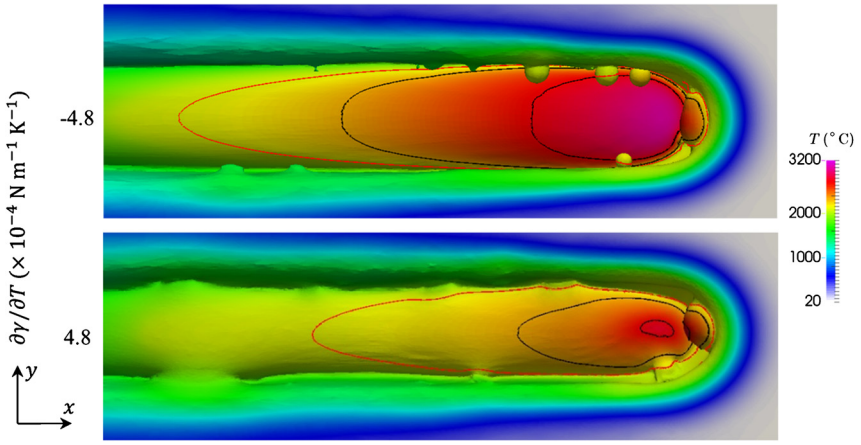

Fig. 5. Top view of temperature field and iso-contours corresponding to $T = 2104$ (red), 2300 and 2700 °C when the laser arrives to the position $x =$ 1.42 mm.

value. With a high negative $\partial\gamma/\partial T$, a clear centrifugal convection flow can be noticed, with high velocity from the hot centre to the colder boundary under the laser spot. Two opposite convection cells are shown in the transversal cut view (Fig. 4). Note that these two cases show different melt pool shapes, which is related to the expansion (respectively contraction) effect of negative (respectively positive) $\partial\gamma/\partial T$. Another effect is the longer and wider melt pool obtained with negative $\partial\gamma/\partial T$. This is fully consistent with the transport of the high-temperature fluid (see also next paragraph). However, in both cases, the Marangoni convection is limited, affecting a small depth due to the rather high liquid viscosity of liquid alumina (as compared to the one for metals). In both cases, one can notice the formation of liquid droplets. It is caused by the melting of powder and spheroidization under surface tension. Melt pool instability may be generated when these droplets collapse into the main melt pool.

As heat transfer in the melt pool is influenced by the convection flow inside, the melt pool dynamics results in different temperature distributions. The temperature fields with different $\partial\gamma/\partial T$ are shown in Fig. 5. In line with the preceding comparisons regarding the extension of the melt pool, the axial temperature gradient at the rear of the melt pool is reduced for a positive $\partial\gamma/\partial T$. Another remarkable effect is the significant decrease of the maximum temperature, down to about 2700 °C for a positive $\partial\gamma/\partial T$.

3.2.2. Track and layer surface shape

The direct result of melt pool dynamics is the track shape after solidification. Regular and repetitive track is essential in additive manufacturing. However, track irregularities are often observed in the SLM process after solidification. A severe situation is the balling effect, which results in poor track regularity and affects the quality of additive manufacturing. Fig. 6 shows the appearance of balling when increasing the scanning speed from 400 to 600 mm s^{-1}. The track is not continuous any more, but broken into isolated islands. These islands are periodically developed along the scanning trajectory. The height map shows that the maximum height of islands is about 50 µm, which is close to the layer thickness. The zone between

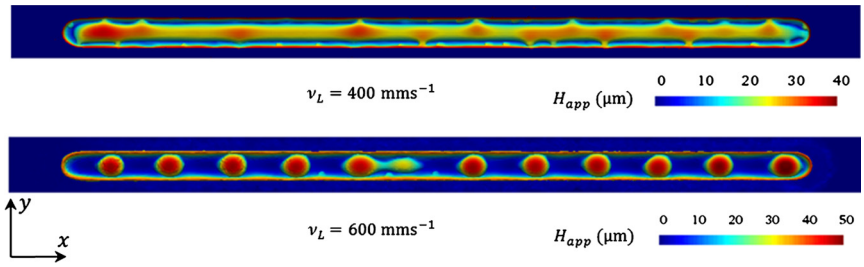

Fig. 6. Colour map of single-track height H_{app} (with respect to the substrate surface) with different scanning speeds v_L. The track length is 2.6 mm.

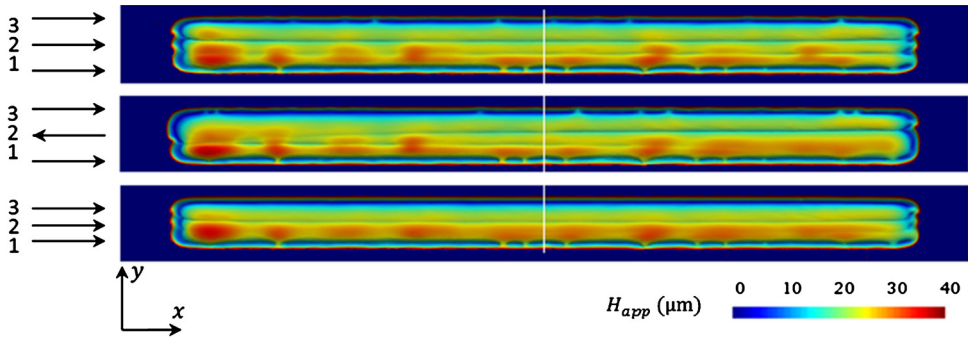

Fig. 7. Colour map of layer height after three passes with different scanning directions (arrows on the left-hand-side part) and hatch distances Δy. The hatch distance is equal to $\Delta y = 50$ µm for the top and central cases and $\Delta y = 40$ µm for the bottom case. The length of each track is 2.6 mm.

isolated islands is slightly over the initial substrate surface. This means that the liquid above the substrate is cleaned up and gathered together by surface tension to form these islands.

In order to obtain the desired layer surface, different scanning strategies can be used, for example, by combining the scanning direction and the hatch distance Δy. These two factors are investigated in Fig. 7. Differences can be noticed between juxtaposed tracks. For unidirectional scanning (top case) with $\Delta y = 50$ µm, there is a clear boundary in the shape of the groove, between tracks. With zigzag strategy (central case), two regimes can be distinguished. The first regime corresponds to the transition region when the laser turns back between two successive passes. Two tracks are then connected without visible boundary. The boundary appears again out of this region and the surface looks similar to the previous case. The decrease of the hatch distance to 40 µm (bottom case) consists in increasing the overlap between the juxtaposed tracks. This leads to a boundary almost invisible: the two first tracks appear as a wider single track due to the partial remelting of the initial track and merge with the second track. However, a boundary appears between the second and third tracks, rather than being smoothly connected. All three cases show the decrease of surface height fluctuation from the first to the last track, showing the influence of previous solidified tracks on the surface morphology.

The profile evolution of the gas/material interface ($\psi = 0$) in the median cross section (white line in Fig. 7) is plotted in Fig. 8, taken at the end of each pass. In fact, the profiles obtained with unidirectional and zigzag scanning are almost the same, so only one of them is given. Along the lateral sides of the developed track, there is still some powder in contact with the track. Due to weak overlap with $\Delta y = 50$ µm and the concave shape of track section, the groove between the first and second tracks can be clearly observed. This does not appear with $\Delta y = 40$ µm, and a smoother surface is obtained. The height of the second track is lower than the first with $\Delta y = 50$ µm, but they are almost the same with $\Delta y = 40$ µm. The third track is more expanded in the width (direction y) and the groove appears in all cases. In fact, under the surface tension effect, the melt pool tends to be attracted by the previously solidified track. A slight nonphysical displacement of the interface is noticed. The profiles of the first track slightly change during the three passes (from 200 µm to 250 µm in Fig. 8), which is mainly caused by successive transport after remeshings.

3.3. Solid thermomechanics

As cracks occur mainly in the yz plane, the stress component σ_{xx} is shown in Fig. 9 for two heating modes. The top is a standard mode with the use of a unique laser beam in charge of the fusion. In the zone affected, just ahead of the laser, the increase of temperature results in a decrease of the density, leading to thermal expansion. Hence, compressive stress is formed as the expansion of material is inhibited by the surrounding material. At the rear of the melt pool, the material solidifies below 2004 °C. Tensile stress is generated during cooling as the material tends to shrink but is inhibited by the surrounding. The maximum of σ_{xx} attains 3 GPa, evidencing the unavoidable occurrence of cracks as the tensile strength of alumina is around 300 MPa. This occurrence of regular cracks may also affect afterward the stress field onto the tracks surface. In the bottom case, an auxiliary laser is used in tandem with the first one, located 250 µm behind the principal

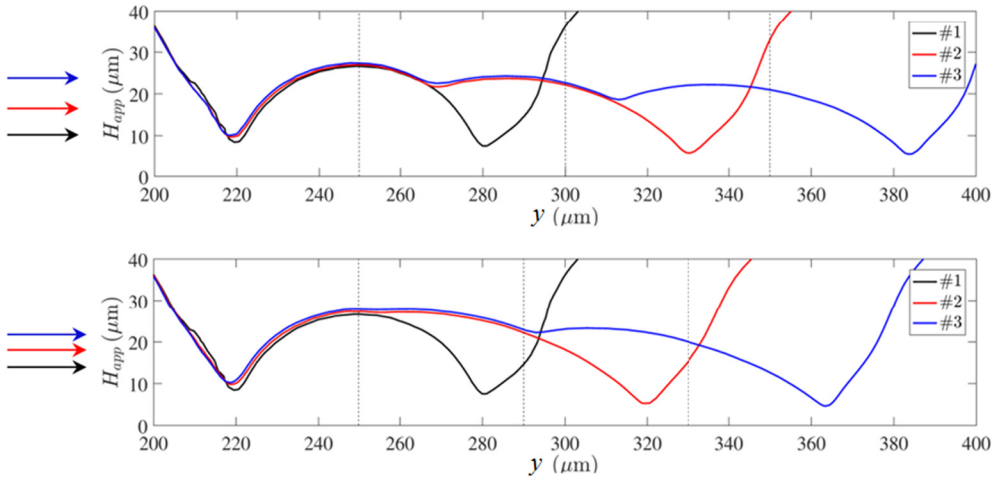

Fig. 8. Profile of the gas/material interface in the cross section (white line in Fig. 7) at the end of each pass (#1–3) for unidirectional scanning (top and bottom simulations in Fig. 7) with hatch distance (top) $\Delta y = 50$ μm and (bottom) 40 μm. The vertical dashed lines indicate the laser scan line for each pass.

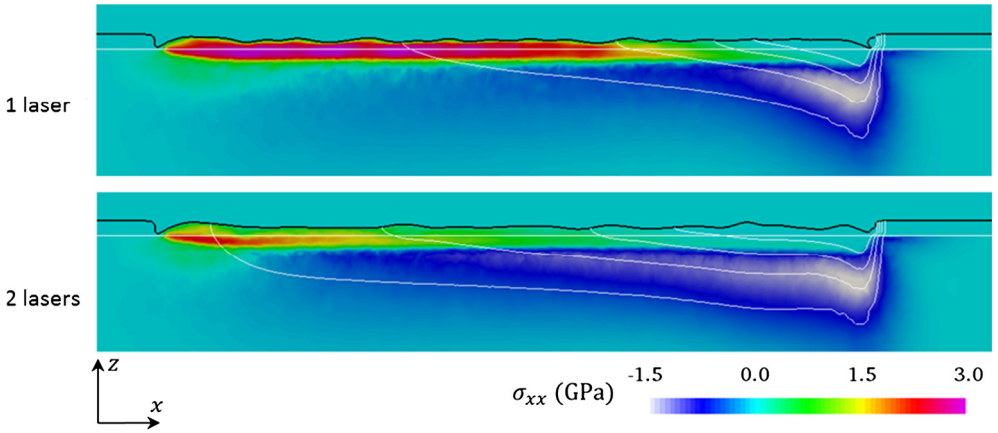

Fig. 9. Stress distribution σ_{xx} when the laser arrives at position $x = 2.6$ mm. The black and horizontal white lines indicate the gas/material and initial powder/substrate interfaces, respectively. White iso-contours correspond to $T = 500$, 1000, 1500, and 2004 °C. The top case corresponds to a unique fusion laser, while an auxiliary laser is used in the bottom case, located 250 μm behind the principal one.

one. This value is proposed in the present simulation as corresponding approximatively to the melt pool length. Both lasers are of the same type, but the second one affects a larger region with $r_{\text{int}} = 200$ μm and its effective power is reduced to $P_{\text{L}}(1 - R) = 60$ W compared to the main laser ($P_{\text{L}} = 84$ W). According to the simulation, this treatment reduces the thermal gradient as temperature isocontours are elongated in the x direction. As a result, σ_{xx} is significantly decreased with a maximum value around 1.5 GPa.

The variation of σ_{xx} along the scanning direction (x) can be noticed in Fig. 9 in the case with a single laser. Stress profiles are thus plotted (Fig. 10) along the x direction at the initial powder/substrate interface in the median longitudinal plane (horizontal white line in Fig. 9). The track height (blue, scale on the right) is also plotted in order to reveal its relation with local stress. One can see the increase of stress during cooling and the much higher stress in direction x than in other directions. A remarkable finding is the correlation between the local stress (for all components) and the local track height (or width). The stress peaks of σ_{xx}, σ_{yy}, and σ_{zz} correspond to the lower and narrower track necks and vice versa. This means that stress concentration can be generated in track necks. Consequently, tracks with stable transverse section are certainly favourable from the point of view of a regular and stable additive construction, but also regarding the minimization of crack risk during construction.

4. Macro-scale modelling at the scale of the part being built

Obviously, the mesoscale approach previously presented is not sustainable at the scale of a whole part. Instead, a macroscale approach is introduced here, including a simplified approach for both energy input and material addition. This approach is based on more macroscopic additions at the scale of entire layers, or fractions of layers, providing a com-

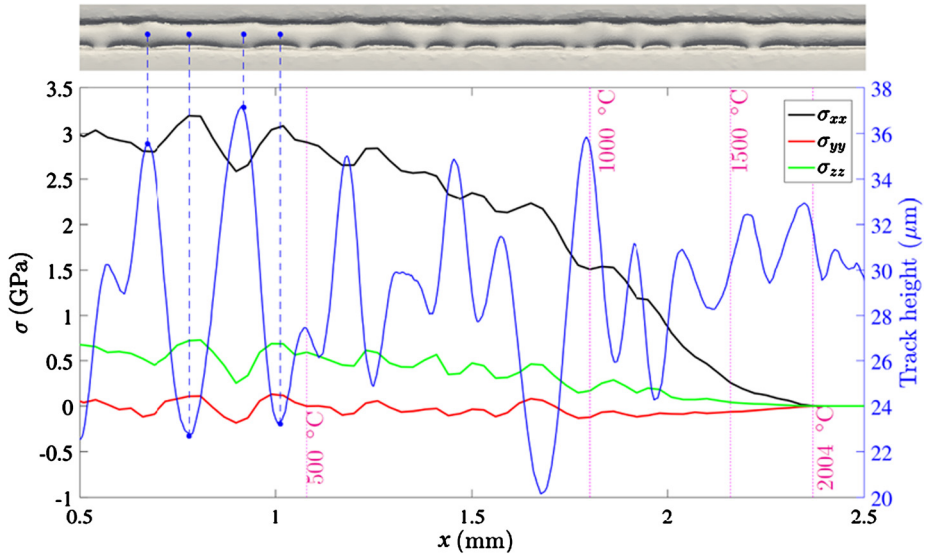

Fig. 10. Single laser case. Stress distribution σ_{xx}, σ_{yy}, and σ_{zz}, and track height (right y axis) along profile (horizontal white line in Fig. 9). A top view of the track (with non-melted powder) is given at the top of the figure. Note that temperature increases along x, the laser being located at $x = 2.6$ mm.

promise between accuracy and computational efficiency. Details of the present modelling are provided in Zhang et al. [16]. The following section is restricted to its main features.

4.1. Concept of deposition layer by layer or by layer fractions

As shown in Fig. 11, the construction plan of a part can be decomposed into several fractions in each layer. In practice, this decomposition may be based on a limit value for the scanned length in any fraction: $l^{\mathrm{lf}}_{\mathrm{scan}}$. Such a user-defined parameter, $l^{\mathrm{lf}}_{\mathrm{scan}}$, reflects the desired balance between computational accuracy and computational time. For instance, fixing this parameter at a very high value (of the order of the time required to treat a full layer) will result in a deposition full layer by full layer. Conversely, taking low values for this parameter (of the order of a few laser beam diameters) would result in a large number of layer fractions inside each layer: the model would tend to degenerate into a smaller scale simulation in which the laser scan path is accurately reproduced. More details can be found in reference [16].

Each layer fraction is supposed to be heated during a short time interval t_{heat}. The latter is estimated from the laser radius and scanning velocity and corresponds to the time duration during which the material is exposed to the laser radiation. Note that this time duration does not depend on of the layer or layer fraction considered. Layer fractions are assumed to be heated homogeneously throughout their thickness. Accordingly, a simple energy balance leads to the expression of the heat source term to be implemented as the right-hand side of Eq. (4):

$$\dot{Q}_{\mathrm{L}} = \frac{P_{\mathrm{L}}(1-R)t^{\mathrm{lf}}_{\mathrm{scan}}}{S_{\mathrm{lf}}t_{\mathrm{heat}}\Delta z_{\mathrm{t}}} \tag{18}$$

where Δz_{t} is the powder bed thickness, and $t^{\mathrm{lf}}_{\mathrm{scan}}$ and S_{lf} are the scan time and the surface of the considered layer fraction, respectively.

Cooling is afterwards simulated during the residual time, $t^{\mathrm{lf}}_{\mathrm{cool}}$, defined as $t^{\mathrm{lf}}_{\mathrm{scan}} - t_{\mathrm{heat}}$ (Fig. 11). This approach is repeated till all the various fractions of layers are consecutively melted. When the scanning of a given layer is ended, a new coating of powder is added, which is simulated by the updating of the level-set function ψ, as mentioned in Section 1.2, and cooling is simulated during a certain dwell time to spread a new powder bed layer at the top of the construction. The simulation procedure is repeated till the end of the process. Each time increment of the procedure consists of a thermal resolution, a mechanical resolution, and a possible remeshing step.

4.2. Application

The present macroscale modelling strategy is applied to a typical impellor structure made of the Ni-based superalloy IN718 with a diameter of 20 mm at the base and a height of 10 mm, as shown in Fig. 12. The limit scanned length is fixed to $l^{\mathrm{lf}}_{\mathrm{scan}} = 56$ mm. Due to the variable section areas of the part, the number of layer fractions per deposited layer varies from 20 layer fractions in the bottom of the part to 4 layer fractions only in the top of the impellor. At any instant of the simulation, the computational domain includes the metallic material (substrate and already-built fraction of the final part), the gas and the non-irradiated powder.

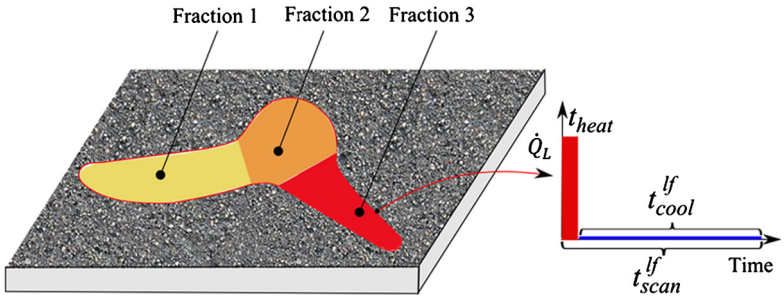

Fig. 11. Decomposition of a single powder layer into several fractions to be heated consecutively.

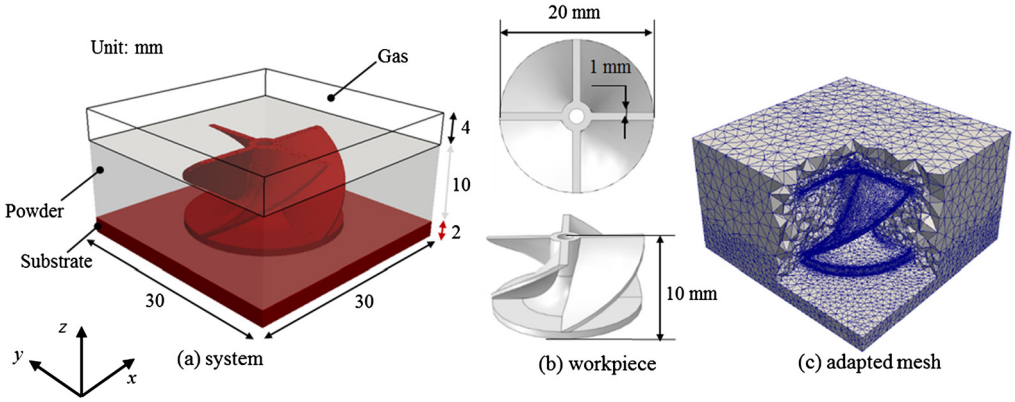

Fig. 12. Case configuration and adapted mesh for the final geometry.

To maintain computational efficiency, the FE mesh is regularly adapted during the construction process. The adaptation strategy is globally based on the updated two-level sets as given in Fig. 1b, and on predefined rules such as keeping a fine mesh near the construction front of the piece, while coarsening the mesh far from the construction front and deep into the non-irradiated powder. Such characteristic features can be observed in Fig. 12c, where the finite element mesh is shown close to the end of the construction process. As a result, the mesh contains around 2 million elements. The thermo-mechanical analysis is performed all along the construction process, including a total of 50 layers. It is then continued during the cooling process to room temperature, during 3 h. The constructed part is then removed from the substrate. The temperature evolution during and following the construction, the residual stress and distortion after cooling down to room temperature and removing from the substrate are presented in the following subsections.

4.2.1. Heat transfer in constructed part and non-irradiated powder

For the thermal analysis, a convective heat exchange boundary condition is considered along the bottom and lateral surfaces of the domain, while an adiabatic condition (null heat flux) is assumed along the boundaries of the gas domain on the top surface, see [16] for details. Compared to this previous work, the porosity of the powder is here taken as 52%, and the dwell time is extended to 17 s, which is more representative of the real process. In Fig. 13, temperature distributions are given in the assembly part plus the non-irradiated powder and in the constructed part alone. In Fig. 13a and c, the elements located in the gas domain are not present. In practice, elements such as $\mathcal{H}(\psi) < 0$ are not represented. The same treatment is applied in Fig. 13b and d, where, in addition, elements such as $\mathcal{H}(\psi) > 0$ and $\mathcal{H}(\varphi) < 0$ are eliminated (non-irradiated powder elements). For the non-irradiated powder near the constructed part, temperature keeps around 300 °C, so the consideration of the non-irradiated powder is quite important to simulate heat transfer in the whole domain (Fig. 13a). This is all the more important that the powder is confined between part regions, especially in the middle of the central shaft of the part. It can be noted that in the part, below the construction front, the temperature is maintained in the range 250–300 °C.

When the part is completed, the highest temperature in the non-irradiated powder increases to more than 300 °C (Fig. 13c), and the temperature gradient, essentially vertical, is more obvious in the part (Fig. 13d).

4.2.2. Stress build-up in constructed part – Residual stress

After cooling down to room temperature, the residual stress distributions are given first in the part/substrate assembly, and second in the part alone after substrate removal, see Fig. 14. As the distributions of σ_{xx} and σ_{yy} are similar, only σ_{xx} is shown. For the residual stress in the x direction, tensile stresses mainly locate in the substrate and in the bottom of the constructed part (Fig. 14a), while compressive stresses are found in the middle of the blades. When the substrate is removed,

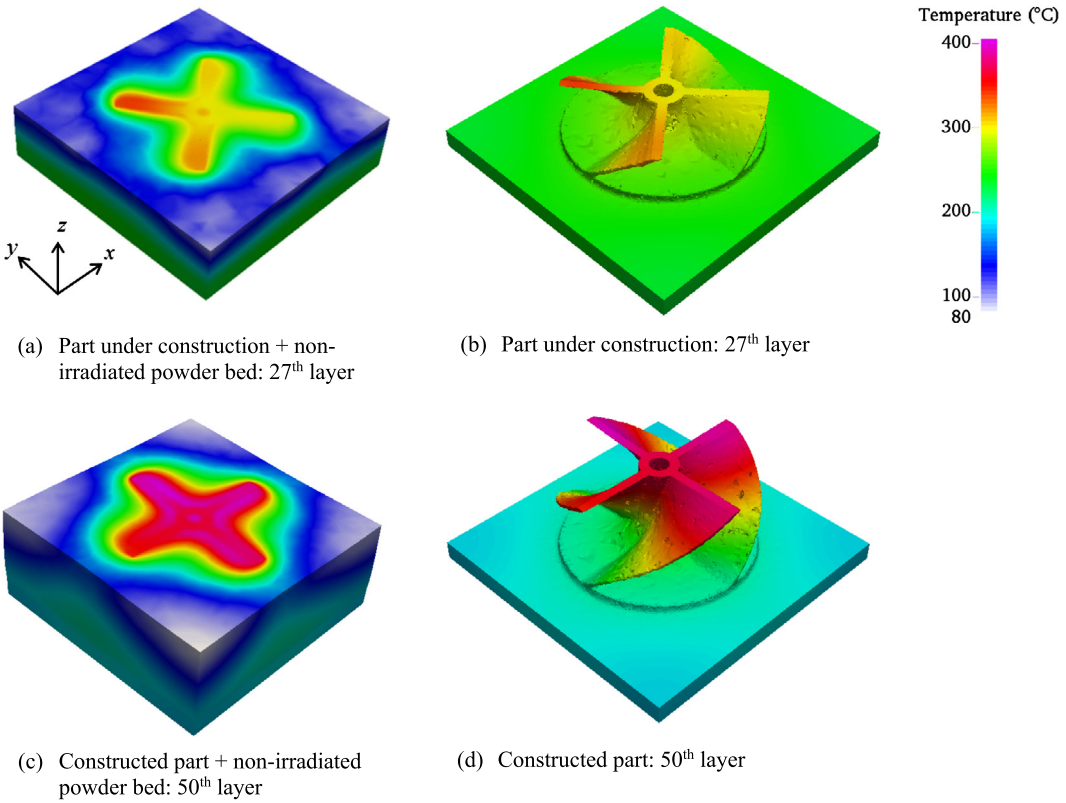

Fig. 13. Macroscale simulation: temperature distribution at an intermediate stage of the construction a) and b), and at the end of the construction c) and d).

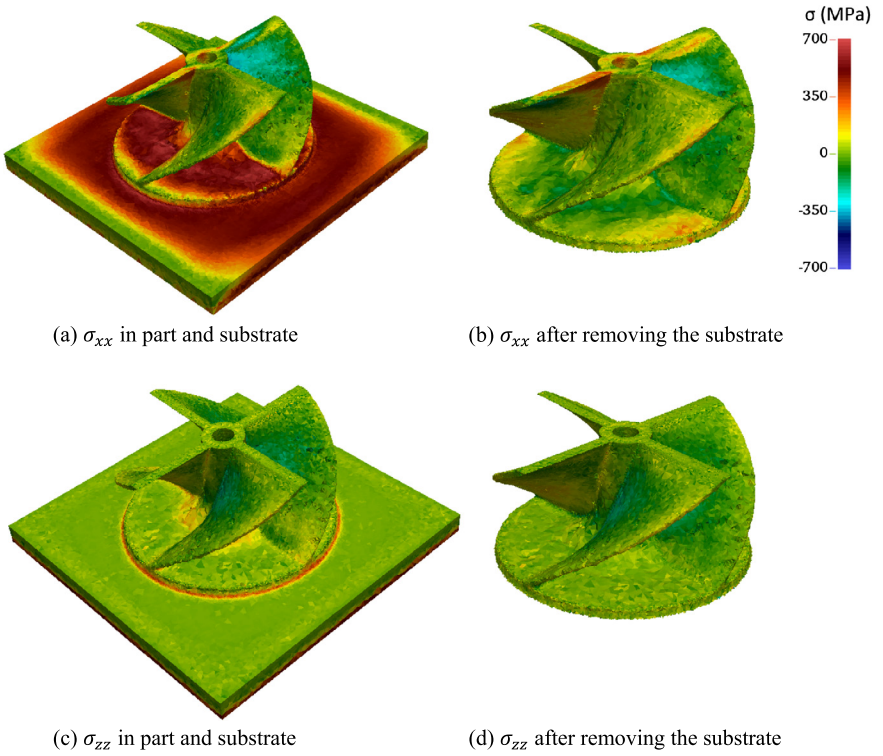

Fig. 14. Residual stress distribution after cooling down to room temperature [left column: a) and c)], and after substrate removal [right column: b) and d)].

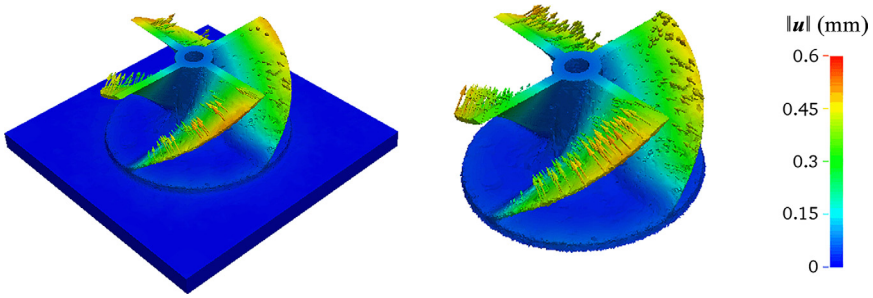

Fig. 15. Distortion distribution after cooling down to room temperature. Colour map of the distribution of the norm of the displacement, with associated nodal displacement vectors (arrows length is proportional to the norm of the vectors).

the stress in the bottom of the part is released to a lower level. The simulation of the removal process consists of two operations. Firstly, the mechanical properties of the substrate material are changed to the properties of a Newtonian material with a low viscosity. Secondly, the displacement field associated with this modification is analysed by releasing gradually the boundary conditions applied to the lower face of the substrate. Proceeding in this way, the mechanical resolution allows finding the final configuration of the part after separation from the substrate.

As for the residual stress in the z direction, the maximum before substrate removal is found in the transition zone between part and substrate. After substrate removal, stress is significantly reduced in this region of the part, while stresses in the upper regions have negligible changes. Moreover, it is found that the values of residual stress in the z direction are more homogeneous compared to these in the x direction.

4.2.3. Displacement build-up in constructed part – Distortion

The distortion for the constructed part after cooling down to room temperature is given in Fig. 15. The norm of the displacement $\|\mathbf{u}\|$ is represented before and after the substrate is removed. Maximum and minimum values are around 0.6 mm (Fig. 15a–b) and are located at the top ends of the blades. It can be noticed that, for this impellor configuration, the distortion distributions of the constructed part show slight difference before and after the substrate is removed.

5. Discussion

In light of the above descriptions, a discussion is given that aims at comparing the meso- and macroscale models. This part is structured considering solvers for conservation equations, inputs/outputs, tracked boundary, remeshing and computational times. Most of the comparisons are summarized in Table 2.

Track/part construction. From the above illustrations of the models, the main difference is obvious. The models do not apply at the same scales. While the macroscopic approach aims at reaching a description of heat flow and mechanical behaviour at the scale of the whole part, the mesoscopic approach is limited to a few tracks, each track being restricted to small length. On the other hand, the mesoscopic model integrates more physical phenomena, and is the basis for integrating even more physical phenomena in the future. This will be discussed in the perspective of the present session. Ideally one would wish to simulate the whole part with the mesoscopic approach. This is yet impossible as will be discussed later when considering the required computational resources. The macroscopic approach thus becomes essential when outputs are required that need to tackle the part and the process, e.g., for predicting residual stresses or geometrical features or defects due to accumulation of hundreds or thousands of layers.

Level set boundaries. A level set is considered with both models that tracks the material/gas boundary. The second level set introduced by the macroscale model tracks the interface between the constructed part and the powder bed. This is achieved by using a conform mesh so as to be as close as possible to the actual geometry and to reduce the need for a very fine mesh on each side of the interface. As a consequence, while it is easy to visualize parts with/without the powder bed with the macro-model, the extraction of the consolidated domain in the mesoscale model requires to filter the information using, e.g., the fraction of powder or gas [15,25]. The description of the interface is less precise with the latter methodology.

Energy conservation. The mesoscale model integrates a volumetric heat source (Eqs. (4) and (15)) that depends on the distance below the material/gas boundary represented by the level-set function. Yet the initial spatial distribution of the heat source at the material/gas boundary is not uniform as it follows a Gaussian distribution. It should be mentioned that the Gaussian-type distribution is not imperative and can be modified easily. This is different in the macroscale model where the heat source is homogeneous in the thickness of the powder bed and uniform throughout the area of each layer fraction. But the main difference between the energy solvers is due to the absence of melting and solidification in the macroscale model. It is inferred with this approximation that the size of the melt pool and the time scale for phase transformation involving liquid are both very small compared to the volume of the part and powder bed domains and the time for the diffusion of heat in these domains. Hence the energy required for melting is compensated by the latent heat released during solidification and can well be neglected when conducting an analysis at the macroscale. Hence the outputs do not include

Table 2
Summary of comparisons between the meso- and macroscale models.

Scale	Meso	Inputs(**I.**)/Outputs(**O.**)	Macro	Inputs(**I.**)/Outputs(**O.**)
Typical construction	Few parallel tracks	**I.** Linear segments with scan direction **O.** Track shape	Full part geometry	**I.** CAD model (e.g., G-code) **O.** Part geometry
Level-set boundaries (Eq. (3))	Yes One boundary	**I.** Parameter for interface modelling (Eq. (1)) **O.** Material/gas	Yes Two boundaries	**I.** Parameters for interface modelling (Eq. (1)) **O.** Material/Gas part/Powder bed
Energy conservation (Eq. (4))	Yes	**I.** Volumetric heat source, thermal properties (Eqs. (15)–(16)), solidification path, fluids velocity **O.** Temperature and phase distributions	Yes	**I.** Volumetric (uniform) heat source (Eq. (18)), thermal properties [16] **O.** Temperature distribution
Total mass conservation (Eq. (5))	Yes	**I.** Material densities **O.** Fluid flow	No	
Fluid mechanics (Eq. (6))	Yes	**I.** Liquid and gas properties, liquid/gas interface properties (Eqs. (7) and (17)), temperature field **O.** Fluid flow, track shape, material/gas surface roughness	No	
Solid mechanics (Eq. (9))	Yes	**I.** Parameters for elastic–viscoplastic behaviour (Eqs. (11)–(12)) **O.** Stress and strain in the track neighbourhood	Yes	**I.** Parameters for elastic–viscoplastic behaviour (Eqs. (11)–(12)) **O.** Distortion and residual stresses in the part
Mesh adaptation	Yes	**I.** Level-set parameters, density, liquid fraction, heat source distribution, temperature **O.** Refined mesh at boundary and according to various fields	Yes	**I.** Level-set parameters **O.** Conformed mesh at boundaries

the distribution of phases and the solidification path. While these data are required for mesoscale modelling, they are not necessary for the macroscale modelling.

Total mass conservation and fluid mechanics. These equations are only solved by the mesoscale model, providing output with fluid flow, change of material volume upon melting and consolidation of the powder (as the powder is a homogeneous domain with an equivalent density), track shape including the possibility to predict surface roughness and balling. One should notice that these outputs are essential for calibrations. Indeed, selection of processing parameters for an additive manufacturing first start with single tracks generations as a function of power, velocity and other heat source features. Similarly, sensitivity to several defects is also evaluated with such simple tests. Availability of a calibrated physically based model for such studies is imperative.

Solid mechanics. Prediction of stresses and strains at the consolidated regions are developed based on the same solver. However, they aim at providing different outputs. For the macroscale model, the goal is to predict distortion and residual stresses in the whole part. The geometrical dimensions may then be checked, as well as the risk for cracking during construction or cooling to room temperature. In addition, the final geometry of the whole part is predicted and may be compared to the CAD model. This provides information on possible optimization of the SLM strategy in order to minimize distortions. Oppositely, tracking of the pool with the mesoscale model can be oriented toward hot tearing, i.e. a metallurgical defect that is linked to phase transformation. The occurrence of cracks may be estimated as well as defect orientation depending on main stress directions.

Remeshing strategies. Remeshing strategies are first developed to track domain boundaries. For the macroscale model, this is done by defining a fine mesh close to the deposited layer and progressively making it coarser with the distance to the construction front. At the same time, a conform mesh is kept at the boundary between the part and the powder bed. This second strategy avoids artificial loss of the geometrical contours of the part due to successive remeshing over time and also significantly reduces the number of elements compared to a standard level-set-based front-capturing remeshing strategy. The remeshing strategy for the mesoscale model does not only aim at tracking the boundary between the material and the gas, but also at refining the mesh where large gradients (or more precisely second order spatial derivatives) develop. For instance, variables such as the density, the liquid fraction, the heat source distribution, and the temperature are also considered. This permits refining the gas/material interface, the melt pool boundary, the region impacted by the laser and the region with high variation of the temperature gradient, respectively. In both models, isotropic and anisotropic metrics are continuously calculated during the simulations and communicated to the remeshing procedure in charge of updating the nodal positions and the mesh topology.

Time integration. This is certainly one of the main differences between the models. Classical time integration is achieved using the mesoscale model: successive resolutions of energy, fluid mechanics, transport of the level set, solid mechanics, and remeshing are performed [25]. Because of the physical phenomena to capture (fluid flow of the order of laser velocity, i.e. 0.3 $\mathrm{m\,s^{-1}}$), a smooth simulation of the fluid flow and its instabilities requires small time steps. Estimation can be achieved by using the track width as a representative size, i.e. a few tens of µm. One thus finds a time scale of typically hundreds of µm, i.e. time steps of the order of the µs. Optimization can be made by identifying physical phenomena that do not proceed with the same time scale. For instance, one could reduce the number of resolution for solid mechanics with a larger time step, as suggested by Bellet et al. [29]. In macroscale simulations, as the flow in the melt pool is not solved, the time step limitation seems not so drastic. What limits the time step is actually the heating of each layer or layer fraction. As explained above, the heating time is the time during which the material is exposed to the laser radiation. A simple estimation consists of the ratio $t_{\mathrm{heat}} = 2r_{\mathrm{int}}/v_{\mathrm{L}}$. Taking $2r_{\mathrm{int}}$ and v_{L} of the order of 75 µm and 0.3 $\mathrm{m\,s^{-1}}$, respectively, t_{heat} is of the order of a few hundreds of µs. Zhang et al. [16] demonstrated that t_{heat} could be multiplied by a certain factor – up to 40 – without affecting significantly the results. Besides, during cooling of each layer or layer fraction, or during dwell time, the time step can be considerably larger than t_{heat}. In total, this allows relaxing time step limitations and maintaining sustainable computational time for the macroscopic approach.

Computational times. Computational time per unit length can be computed for both models. It reaches 0.05 $\mathrm{day\,m^{-1}}$ for the macroscale model and 1300 $\mathrm{day\,m^{-1}}$ for the mesoscale model. In fact, with a total distance travelled by the laser of 70 m, the simulation of the part shown in Fig. 12 with the mesoscale model could be estimated to 250 years. This means that a simulation of the whole part with a mesoscale model is currently out of reach, even with supercomputers.

6. Conclusion

Thermomechanical analyses for additive manufacturing are performed with meso- and macroscale models. Both analyses include a combination of the level-set methodology and remeshing strategies to follow the deposited track and the construction by layers. The main difference between the models is the melt pool simulation, detailed with the mesoscale model while omitted with the macroscale model.

In the mesoscale model, the fluid dynamics in the melt pool caused by opposite temperature surface tension coefficients is discussed. This coefficient is shown to have significant influence on the length and width of the melt pool. The fluid dynamics and solidification result in the final track shape and its surface roughness. While very high scanning speed at constant heat source power is known to prevent melting, intermediate value leads to the balling effect as demonstrated by the mesocale model. For multiple track deposition, it is shown that the shape of the layer surface is more sensitive to the hatch distance than to the scanning direction, as the latter only modifies the transition region between successive tracks. At the end, simulations show that the maximum tensile stress can be reduced by using an auxiliary laser that heats the tail of the melt pool. In addition, stress concentration may occur with irregular tracks, higher stress being found in the regions with smaller cross sections.

In the macroscale model, a typical impellor part is simulated with input geometrical description directly imported from the CAD software. Two main findings are achieved through the analyses of the simulation. At first, the temperature of the non-irradiated powder near the constructed part is maintained at a high level during processing. This demonstrates the importance of accounting for both the consolidated part and the powder bed during the whole thermomechanical simulation. After cooling down to room temperature, it is also shown that the residual stresses in the vertical direction are more homogeneous compared to these in the horizontal directions, while the maximum distortions in both vertical and horizontal directions are located in the blades.

The presentation of the models, their illustration, and the discussion can be used to draw perspectives for further developments. The first possible additional developments concern the mesoscale model. Modelling of the key hole and more generally a deeper implementation of the interaction of the laser with the material is feasible as already shown in the welding process [30]. Similarly, one could couple the melt pool solidification with the description of metallurgical features, such as the grain structure and its associated texture as previously done in welding simulations [31]. More ambitious is the prediction of porosity and denudation, two defects that are well recognized in the additive manufacturing but not yet tackled. As it is clear that both methodologies present drawbacks and advantages, construction of a modelling chain could also be considered. The mesoscale model would then serve to feed the macroscale model. For instance, after calibration of mesoscale model on a set of experimental data, one could calibrate the heat source that enters the macroscale model so as to retrieve the heat flow computed with the mesoscale model. While this work is tedious, it could then open the door to quantitative macroscale simulations while maintaining simplifications. As explained above, this is the only way to tackle large domain simulations with reasonable computational resources. Beyond model developments, work is in progress for comparison with experimental characterizations. This is one key to reach model calibration and predictive value of the simulations.

Acknowledgements

Part of this work has been conducted within the framework of the CEFALE project, part of the ACLAME program funded by the Institute CARNOT M.I.N.E.S (Paris, France).

References

[1] B. Zhang, Y. Li, Q. Bai, Defect formation mechanisms in selective laser melting: a review, Chin. J. Mech. Eng. 30 (2017) 515–527.
[2] C.Y. Yap, C.K. Chua, Z.L. Dong, Z.H. Liu, D.Q. Zhang, L.E. Loh, S.L. Sing, Review of selective laser melting: materials and applications, Appl. Phys. Rev. 2 (2015) 041101.
[3] C. Körner, E. Attar, P. Heinl, Mesoscopic simulation of selective beam melting processes, J. Mater. Process. Technol. 211 (2011) 978–987.
[4] A. Rausch, V. Küng, C. Pobel, M. Markl, C. Körner, Predictive simulation of process windows for powder-bed fusion additive manufacturing: influence of the powder bulk density, Materials 10 (2017) 1117.
[5] W. King, A.T. Anderson, R.M. Ferencz, N.E. Hodge, C. Kamath, S.A. Khairallah, Overview of modelling and simulation of metal powder-bed fusion process at Lawrence Livermore National Laboratory, Mater. Sci. Technol. 31 (2015) 957–968.
[6] C. Qiu, C. Panwisawas, M. Ward, H.C. Basoalto, J.W. Brooks, M.M. Attallah, On the role of melt flow into the surface structure and porosity development during selective laser melting, Acta Mater. 96 (2015) 72–79.
[7] M. Megahed, H.W. Mindt, N. N'Dri, H. Duan, O. Desmaison, Metal additive-manufacturing process and residual stress modeling, IMMI 5 (4) (2016) 1–33.
[8] H.W. Mindt, M. Megahed, N.P. Lavery, M.A. Holmes, S.G.R. Brown, Powder bed layer characteristics: the overseen first-order process input, Metall. Mater. Trans. A 47 (2016) 3811–3822.
[9] S. Ly, A. Rubenchik, S. Khairallah, G. Guss, M. Matthews, Metal vapor microjet controls material redistribution in laser powder-bed fusion additive manufacturing, Sci. Rep. 7 (2017) 4085.
[10] D. Gu, B. He, Finite element simulation and experimental investigation of residual stresses in selective laser melted Ti–Ni shape memory alloy, Comput. Mater. Sci. 117 (2016) 221–232.
[11] N.E. Hodge, R.M. Ferencz, J.M. Solberg, Implementation of a thermomechanical model for the simulation of selective laser melting, Comput. Mech. 54 (2014) 33–51.
[12] M.F. Zaeh, G. Branner, Investigations on residual stresses and deformations in selective laser melting, Prod. Eng. Res. Dev. 4 (2010) 35–45.
[13] P. Alvarez, J. Ecenarro, I. Setien, M.S. Sebastian, A. Echeverria, L. Eciolaza, Computationally efficient distortion prediction in powder-bed fusion additive manufacturing, Int. J. Sci. Eng. Res. 2 (2016) 39–46.
[14] B. Li, C.H. Fu, Y.B. Guo, F.Z. Fang, A multiscale modeling approach for fast prediction of part distortion in selective laser melting, J. Mater. Process. Technol. 229 (2016) 703–712.
[15] Q. Chen, G. Guillemot, C.-A. Gandin, M. Bellet, Three-dimensional finite element thermomechanical modeling of additive manufacturing by selective laser melting for ceramic materials, Addit. Manuf. 16 (2017) 124–137.
[16] Y. Zhang, G. Guillemot, M. Bernacki, M. Bellet, Macroscopic thermal finite element modelling of additive metal manufacturing by selective laser melting process, Comput. Methods Appl. Mech. Eng. 331 (2018) 514–535.
[17] S. Osher, J.A. Sethian, Fronts propagating with curvature dependent speed: algorithms based on Hamilton–Jacobi formulations, J. Comput. Phys. 79 (1988) 12–49.
[18] M. Shakoor, Three-Dimensional Numerical Modeling of Ductile Fracture Mechanisms at the Microscale, PhD Thesis, Mines ParisTech, France, 2016.
[19] A. Saad, C.-A. Gandin, M. Bellet, Temperature-based energy solver coupled with tabulated thermodynamic properties – application to the prediction of macrosegregation in multicomponent alloys, Comput. Mater. Sci. 99 (2015) 221–231.
[20] Y. Zhang, A. Combescure, A. Gravouil, Efficient hyper-reduced-order model (HROM) for thermal analysis in the moving frame, Int. J. Numer. Methods Eng. 111 (2017) 176–200.
[21] E. Hachem, B. Rivaux, T. Kloczko, H. Digonnet, T. Coupez, Stabilized finite element method for incompressible flows with high Reynolds number, J. Comput. Phys. 229 (2010) 8643–8665.
[22] M. Bellet, V.D. Fachinotti, ALE method for solidification modelling, Comput. Methods Appl. Mech. Eng. 193 (2004) 4355–4381.
[23] M. Bellet, O. Jaouen, I. Poitrault, An ALE-FEM approach to the thermomechanics of solidification processes with application to the prediction of pipe shrinkage, Int. J. Numer. Methods H. 15 (2005) 120–142.
[24] L. Moniz, C. Colin, J.-D. Bartout, K. Terki, M.-H. Berger, Laser beam melting of alumina: effect of absorber additions, JOM 70 (2018) 328–335.
[25] Q. Chen, Thermomechanical Numerical Modeling of Additive Manufacturing by Selective Laser Melting of Powder Bed – Application to Ceramic Material, PhD thesis, PSL Research University – Mines ParisTech, France, 2018.
[26] I.A. Aksay, J.A. Pask, R.F. Davis, Density of SiO_2–Al_2O_3 melts, J. Amer. Ceram. Soc. 62 (1979) 332–336.
[27] E. Sanchez-Gonzalez, J.J. Melendez-Martinez, A. Pajares, P. Miranda, F. Guiberteau, B.R. Lawn, Application of Hertzian tests to measure stress–strain characteristics of ceramics at elevated temperatures, J. Amer. Ceram. Soc. 90 (2007) 149–153.
[28] P.F. Paradis, T. Ishikawa, Surface tension and viscosity measurements of liquid and undercooled alumina by containerless techniques, Jpn. Soc. Appl. Phys. 44 (2005) 5082–5085.
[29] M. Bellet, O. Boughanmi, G. Fidel, A partitioned resolution for concurrent fluid flow and stress analysis during solidification: application to ingot casting, in: A. Ludwig, M. Wu, A. Kharicha (Eds.), Proc. MCWASP XIII, 13th Int. Conf. on Modelling of Casting, Welding and Advanced Solidification Processes, Schladming (Austria), 17–22 June 2012, in: IOP Conf. Ser., vol. 33, 2012, 012052.
[30] W. Tan, Y.C. Shin, Multi-scale modeling of solidification and microstructure development in laser keyhole welding process for austenitic stainless steel, Comput. Mater. Sci. 98 (2015) 446–458.
[31] S. Chen, G. Guillemot, C.-A. Gandin, Three-dimensional cellular automaton-finite element modeling of solidification grain structures for arc-welding processes, Acta Mater. 115 (2016) 448–467.